The Astrophysical Journal, 889:72 (10pp), 2020 February 1 https://doi.org/10.3847/1538-4357/ab63d0

Drifting Pulsation Structure at the Very Beginning of the 2017 September 10 Limb Flare

Marian Karlický[1], Bin Chen[2], Dale E. Gary[2], Jana Kašparová[1], and Jan Rybák[3]
[1] Astronomical Institute of the Czech Academy of Sciences, Fričova 298, Ondřejov, 251 65, Czech Republic
[2] Center for Solar-Terrestrial Research, New Jersey Institute of Technology, 323 M L King Jr Boulevard, Newark, NJ 07102-1982, USA
[3] Astronomical Institute, Slovak Academy of Sciences, Tatranská Lomnica, Slovakia
Received 2019 November 18; revised 2019 December 17; accepted 2019 December 17; published 2020 January 28

Abstract

Drifting pulsation structures (DPSs) are important radio fine structures usually observed at the beginning of eruptive solar flares. It has been suggested that DPSs carry important information on the energy release processes in solar flares. We study DPS observed in an X8.2-class flare on 2017 September 10 in the context of spatial and spectral diagnostics provided by microwave, EUV, and X-ray observations. We describe DPS and its substructures that were observed for the first time. We use a new wavelet technique to reveal characteristic periods in DPS and their frequency bands. Comparing the periods of pulsations found in this DPS with those in previous DPSs, we found new very short periods in the 0.09–0.15 s range. We present Expanded Owens Valley Solar Array images and spectra of microwave sources observed during the DPS. This DPS at its very beginning has pulsations in two frequency bands (1000–1300 MHz and 1600–1800 MHz), which are interconnected by fast drifting bursts. We show that these double-band pulsations started just at the moment when the ejected filament splits apart in a tearing motion at the location where a signature of the flare current sheet later appeared. Using the standard flare model and previous observations of DPSs, we interpret these double-band pulsations as a radio signature of superthermal electrons trapped in the rising magnetic rope and flare arcade at the moment when the flare magnetic reconnection starts. The results are discussed in a scenario with the plasmoid in the rising magnetic rope.

Unified Astronomy Thesaurus concepts: Solar flares (1496); Solar radio emission (1522)

1. Introduction

Solar flares classified in soft X-rays (*GOES*) as X-flares belong to the strongest type of flares, thus they are a topic of great interest. The 2017 September 10 X8.3 flare, which was partially occulted by the west limb and peaked at around 16:00 UT, was the second largest solar flare in Solar Cycle 24. It has been studied from various points of view in more than 30 papers to date.

For example, Yan et al. (2018) show that the flare was associated with a flux-rope eruption followed by the plasma inflow with the formation of a current sheet and coronal mass ejection. Analyzing the spectra of high-temperature Fe XXIV lines observed by the Extreme-Ultraviolet Imaging Spectrometer (EIS) in the impulsive phase of this flare, Polito et al. (2018) found that the lines are very broad. They interpret this broadening as caused by the presence of a non-Maxwelian electron distribution. They also estimated the plasma density of the hot plasma component in the flare arcade at 16:59 UT as $(0.9–2.0) \times 10^{11}$ cm^{-3}. Furthermore, based on Expanded Owens Valley Solar Array (EOVSA) and the *Reuven Ramaty High Energy Solar Spectroscopic Imager* (*RHESSI*) observations, Gary et al. (2018) show that the microwave and HXR sources arise from a common nonthermal electron population, although the microwave sources occupy a much larger area. Warren et al. (2018) presented spectroscopic observations of the current sheet in this flare and estimated the emission measure and plasma density in the current sheet as 10^{30} cm^{-5} and 10^{10} cm^{-3}, respectively. Long et al. (2018) studied the coronal cavity around the erupting filament. The magnetic morphology and dynamics of the accompanying coronal mass ejection were studied by Veronig et al. (2018). Omodei et al. (2018) analyzed the gamma-ray emission of this flare, and suggested three phases in acceleration of protons lasting more than 12 hr. Gopalswamy et al. (2018) reported the ground-level enhancement event associated with a coronal mass ejection whose initial acceleration ($\sim$9.1 km s^{-2}) and initial speed ($\sim$4300 km s^{-1}) were among the highest observed by the LASCO coronagraph.

Although the drifting pulsation structure (DPS) was recorded sometimes in older radio spectra (see, e.g., Figure 24 in Isliker & Benz 1994), DPS as a distinct radio burst was established after its physical interpretation in the paper by Kliem et al. (2000). In this paper, based on the observations made by Ohyama & Shibata (1998) and using the numerical modeling of the magnetic reconnection, it was proposed that DPS is a plasma emission signature of the plasmoid formed in the impulsive phase of solar flares.

DPSs occur quite frequently at the beginning of the eruptive solar flares, mainly in the 1000–2000 MHz frequency range (Nishizuka et al. 2015). They consist of many relatively narrowband pulses that show a frequency drift to lower or sometimes higher frequencies as a whole. Their physical origin can be explained within the standard CSHKP flare model (Carmichael 1964; Sturrock 1966; Hirayama 1974; Kopp & Pneuman 1976). Before the flare, a magnetic rope (i.e., current-carrying loop) is formed, owing to shear and vortex plasma flows at the photospheric level. At its bottom part, a cold and dense plasma condenses into the filament. Then this magnetic rope together with the filament somehow becomes unstable, through proposed mechanisms such as the torus or kink instabilities (Kliem & Török 2006; Kliem et al. 2010) and/or a decrease of the stabilizing magnetic force of the above-lying magnetic field lines (Aurass et al. 2011). This loss of stability leads to upward motion of the magnetic rope. Then, the current sheet is formed below this rising magnetic rope. When this current sheet becomes sufficiently narrow, magnetic reconnection starts. Electrons are accelerated at or near the reconnection X-point. They move toward the rising filament and also

downward to the flare arcade. Some of these electrons are then trapped in the upper part of the rising filament or/and in secondary ropes (formed because of the plasmoid instability in the current sheet; Loureiro et al. 2007). These trapped superthermal electrons in the magnetic rope or in secondary ropes can simultaneously generate the X-ray emission by bremsstrahlung (Ohyama & Shibata 1998), microwaves by the gyrosynchrotron mechanism (Kliem et al. 2010), and DPS due to plasma emission. The sources of these emissions associated with the magnetic ropes are designated in observations as plasmoids. (Note that the term "plasmoid" is also used in the plasmoid instability theory in a somewhat different sense). The pulses in DPS are owing to a quasi-periodic acceleration of electrons at the X-point of the magnetic reconnection. During the upward motion of the magnetic rope, the plasma density inside the plasmoid located in the magnetic rope decreases, thus the emission frequency decreases and DPS as a whole drifts to lower frequencies.

After the initial paper by Kliem et al. (2000), DPSs were studied in several later papers (Khan et al. 2002; Karlický et al. 2004; Karlický & Bárta 2007; Bárta et al. 2008a, 2008b), where observational and model details of DPS were presented. Nevertheless, there are still many open questions regarding DPSs, especially on their substructures.

In this paper, using high-time resolution radio spectra (Jiřička & Karlický 2008), we present an example of DPS with clearly seen substructures and very short period pulsations. This DPS at its beginning consists of pulsations in two frequency bands (1000–1300 MHz and 1600–1800 MHz), which are interconnected by fast drifting bursts. Furthermore, DPS reveals substructures as e.g., narrowband continua and positively fast drifting pulses. To provide context, we show the associated spatial and spectral radio observations obtained by EOVSA, as well as EUV and X-ray observations. (Note that such spatial radio observations associated with DPS are presented for the first time.) Finally, we interpret these double-band pulsations at the start of the DPS in the framework of the eruptive solar flare model, together with results of previous observations and numerical simulations of DPS. Our motivation is to describe the DPS, its substructures, and associate phenomena in detail and account for the most remarkable substructure of DPS: two pulsation bands at the beginning of DPS.

The paper is organized as follows. In Section 2 we describe DPS, its substructures, analysis of pulsations and associated observations in radio (EOVSA), EUV, and X-rays. The interpretation is in Section 3. Discussions and conclusions are in Section 4.

2. Observations

For the analysis of the 2017 September 10 flare, SOL2017-09-10, we use observations in radio from the Ondřejov radiospectrograph with the time resolution 0.01 s (Jiřička et al. 1993; Jiřička & Karlický 2008) and EOVSA (Gary et al. 2018), in X-rays from *FERMI* Gamma-Ray Burst Monitor (GBM; Meegan et al. 2009) and *RHESSI* (Lin et al. 2002), and in EUV from *SDO*/AIA (Lemen et al. 2012).

2.1. Spectral Observations of DPS and its Wavelet Analysis

The 1000–1800 MHz radio spectrum observed at the very beginning of the 2017 September 10 flare is shown in Figure 1. Because the emission in this band became so bright as to saturate the Ondřejov spectrograph after 15:54 UT, we limit our discussion to the very early phase of the flare (15:48–15:54 UT), which ends 5–6 minutes before the peak of the impulsive phase (~16:00 UT). The radio emission as a whole during this early time is a classic example of DPS (Kliem et al. 2000; Karlický et al. 2004; Bárta et al. 2008a). It starts at 15:48:12 UT in two frequency bands at about 1000–1300 MHz and 1600–1800 MHz. Then from 15:50:00 to 15:51:30 UT a series of pulsations in the range 1000–1300 MHz drifts toward lower frequencies with a frequency drift rate of about -1.6 MHz s^{-1}. After 15:51:30 UT the pulsations remain within the same frequency range of 1000–1300 MHz superimposed on a strongly brightening continuum covering the entire 1000–1800 MHz band. A detail of the initial radio emission is shown in Figure 2. It is important to see that at 15:48:17–15:48:25 UT the two frequency bands (1000–1300 MHz and 1600–1800 MHz) are interconnected with fast drifting bursts.

On higher frequencies (2–4.5 GHz), the spectrum shows the broadband continuum starting at about 15:48:30 UT; see http://www.asu.cas.cz/~radio/radio/rt4/2017/A1709102.gif. On the other hand, at frequencies below 1 GHz, the e-Callisto (BIR) 200–400 MHz spectrum shows type III bursts and continua, and the e-Callisto (BLENSW) 20–80 MHz spectrum type III and II bursts (http://soleil.i4ds.ch/solarradio/callistoQuicklooks/).

The radio spectrum in Figure 1 was observed with a time resolution of 10 ms. This offers a unique opportunity to search for substructures in this DPS. Examples of substructures at higher time resolution are shown in Figures 3 and 4 (see boxes in Figure 1, which place these panels in the context of the overall emission). Figure 3 shows pulsations in the 1000–1300 MHz range in 30 s time intervals. As seen here, not only does the bandwidth of some pulsations vary, but in some cases their upper- or lower-frequency boundaries drift to higher or lower frequencies. Examples of the substructures in selected 6 s intervals are shown in Figure 4. It is interesting that most pulsations show a positive frequency drift on this timescale, see (Figures 4(b) and (d)). For example, the burst in the 1150–1300 MHz range at 15:49:22.6–15:49:22.7 UT has a drift rate of about 1.5 GHz s^{-1} and the burst in the 1100–1300 MHz range at 15:50:33.75–15:50:33.9 UT a drift rate of about 1.3 GHz s^{-1}. On the other hand, in pulsations in the 1600–1800 MHz frequency range presented in Figure 4(a), no measurable frequency drift was found. However, the whole series of pulsations (15:48:35–15:48:41 UT) slowly drifts toward higher frequencies with the frequency drift ~10 MHz s^{-1}. Figure 4(c) shows a double stripe burst with stripe frequencies of 1080 and 1120 MHz at 15:49:25 UT. See also that this burst is associated with the pulses in the 1700–1900 MHz frequency range. We pay attention to this double stripe burst because it is very bright (700 SFU) and resembles the very bright zebra-like burst shown by Tan et al. (2014). A variety of different substructures (pulsations, narrowband continua, drifting pulses, dot-like bursts) indicates complex electron distribution functions in the DPS source. The drifting pulses could be connected with the beam-like distribution, while the pulsations and narrowband continua with the beam-like or/and with loss-cone distributions.

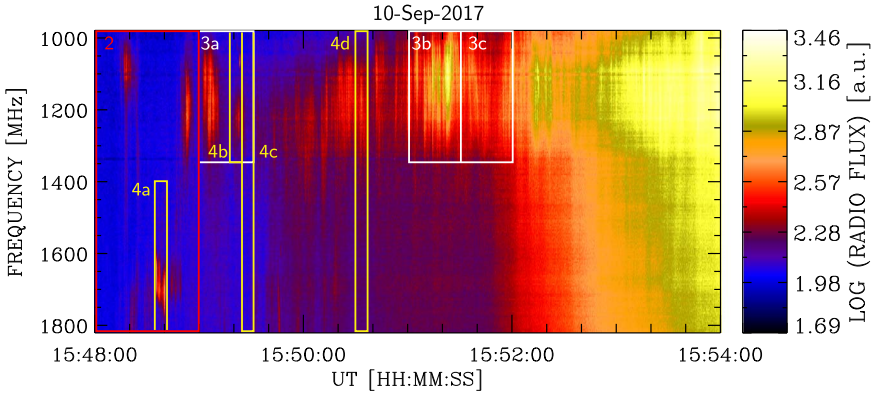

Figure 1. Overview radio dynamic spectrum in the 1000–1800 MHz range observed during the 2017 September 10 flare by the Ondřejov radiospectrograph (Jiřička & Karlický, 2008) at 15:48–15:54 UT. The color boxes outline regions seen at higher zoom level in other figures, and the numbers and letters indicate the corresponding figure and panel numbers.

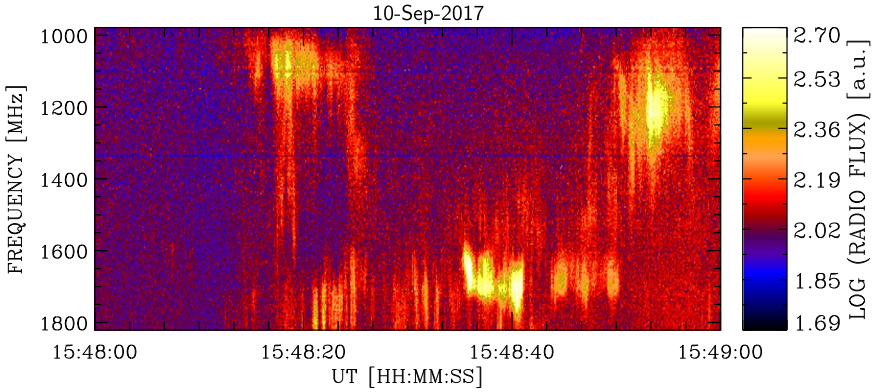

Figure 2. Detail of the radio dynamic spectrum in the 1000–1800 MHz range observed at the very beginning of the 2017 September 10 flare at 15:48–15:49 UT. The pulsations appear mainly in two frequency bands (1000–1300 MHz and 1600–1800 MHz), which are interconnected by fast drifting bursts.

2.1.1. Wavelet Analysis of Pulsations in DPS

As shown in numerical simulations by Kliem et al. (2000), the magnetic reconnection has a quasi-periodic character. Thus, in the magnetic reconnection electrons are accelerated quasi-periodically and generate a quasi-periodic radio emission. To obtain the timescales in the acceleration process in the flare magnetic reconnection in more detail, we analyzed the observed pulsations in the DPS using the wavelet method recently described in Karlický & Rybák (2017). We adopt the Morlet wavelet analysis method with $\omega = 6$. Only periods with 99% significance are presented. This method not only identifies the oscillation periods of the pulsations, but also provides the corresponding phase information. For each time interval in the radio dynamic spectrum that contains DPS features, we calculate a histogram of pulsation periods. Selecting the range of periods at which the histogram peaks, we use the corresponding phase information to identify which features display those dominant periods. The "phase dynamic spectrum" is superposed on the corresponding radio dynamic spectrum, shown in Figures 5 and 6 as pink colors of varying brightness, with black corresponding to zero phase. The time interval between neighboring black lines in these maps indicates the chosen period.

Two examples of our wavelet analysis are shown in Figures 5 and 6. Histograms in these figures show periods from 0.1 up to 2 s. In the lower panel of Figure 5, we show the spectrum with the period of of 0.7–1.1 s which is an example of typical periods found in the analyzed DPS. However, the lower panel of Figure 6 shows the oscillations with much shorter periods of 0.09–0.15 s at 15:48:40–15:48:41 UT in the 1650–1750 MHz frequency band. Some indications of this period is also at 15:48:35.3–15:48:36:3 UT in the 1600–1700 MHz band. The periods around 1 s and longer are common (see, e.g., Kliem et al. 2000; Karlický et al. 2017, 2018), but the periods around 0.1 s in the DPS substructure are new and have not been reported before.

2.2. Associated UV, EOVSA, and X-Ray Observations

In Figure 7, we show the *SDO*/AIA 171 Å observations at the time of double-band pulsations at the beginning of DPS. It is remarkable that at this time the ejected filament is tearing (at about 15:48:20 UT) in the region (the arrow in Figure 7(b)), where at later times a signature of the flare current sheet appeared. At this moment the EOVSA multifrequency radio sources fall along the entire erupting structure, with the lower-frequency contours lying close to the tearing region (Figure 8(a)). About 40 s later, the lower-frequency source (<5.4 GHz) starts to bifurcate into two parts (Figure 8(b)).

Later, the upper part of the ruptured filament moves upward, see the 3.41 GHz red source in the green box in Figure 9(a). Figure 9(a) shows positions of the 3.4–18 GHz radio sources in four regions designated A–D, while Figure 9(b) shows the light curves on 3.41 GHz from these four different regions, marked with a box with the corresponding letter and color in Figure 9(a). Comparing these four sources with the magnetic rope designated by the red dashed line presented in Figure 3 in

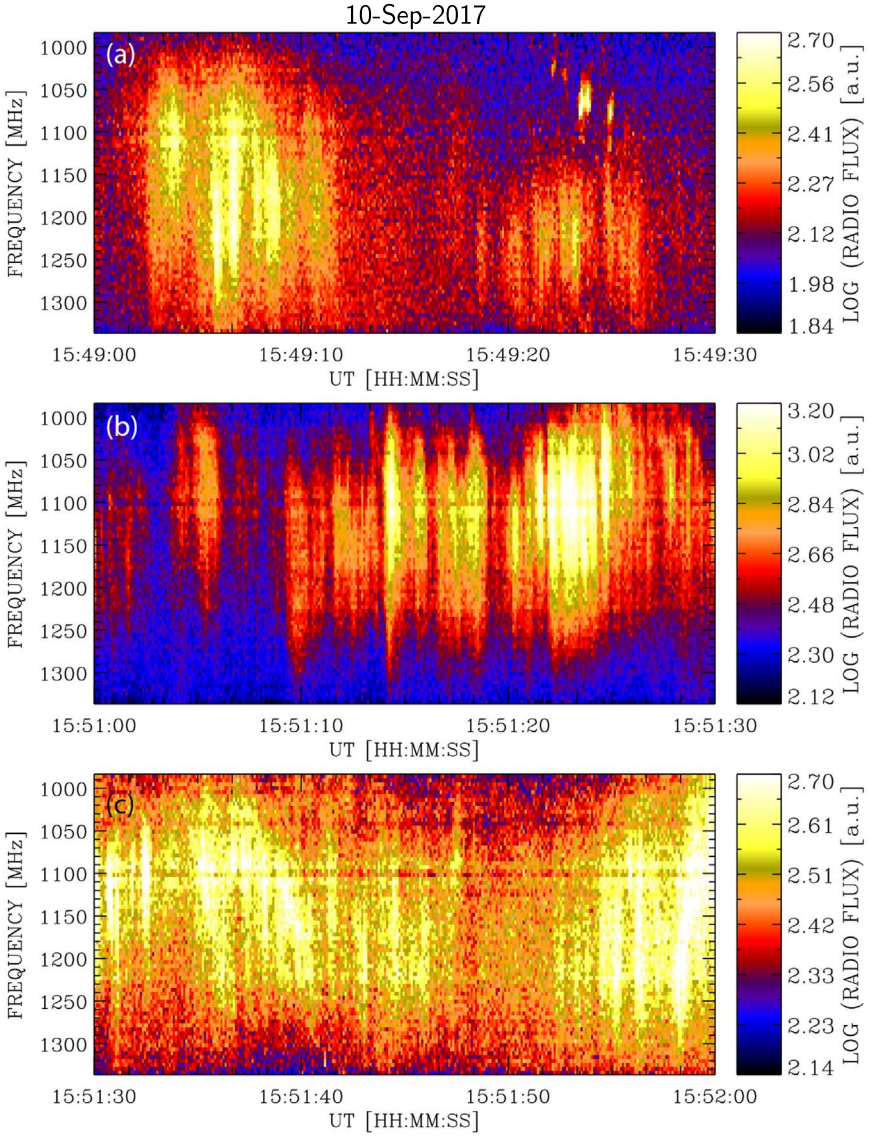

Figure 3. Three examples of the detailed 30 s radio dynamic spectra taken during the 15:48–15:54 UT time interval of the 2017 September 10 flare. See the white boxes labeled 3a, 3b, and 3c in Figure 1.

Yan et al. (2018), source A corresponds to a part of the rapidly rising flux rope observed only on the lowest EOVSA frequencies, source B corresponds to the flare arcade observed in the full EOVSA frequency range (in the cyan box), and sources C and D on either side of the flare arcade coincide roughly with the footpoints of the magnetic rope. After 15:56 UT the green light curve (corresponding to the green box A) is no longer due to the flux-rope source, but is dominated by the emission from the upward-growing arcade source, which encroaches into the green box.

At flare stage, ∼15:52 UT, we also derived the spatially resolved brightness temperature spectra that correspond to each of the four EOVSA microwave sources (Figure 9(c)). The spectrum from source B at the top of the flare arcade is well measured, and is consistent with nonthermal emission, as its peak brightness temperature is above 60 MK. The other sources (A, C, and D) are also possibly nonthermal, inferred from their peak brightness temperature of $\gtrsim$30 MK. The nonthermal nature of these sources, however is less certain, due to having less statistically significant frequency points (filled circles; open circles are data points dominated by noise).

In Figure 10, we compare the EOVSA 3.41 GHz light curves (Figure 9(b)), *FERMI*/GBM 50–100 keV hard emission and the 1000–1300 MHz radio flux corresponding to the main frequency band of DPS. From a global point of view, the DPS 1000–1300 MHz radio flux, 50–100 keV hard X-ray and 3.41 GHz light curves are correlated. As concerns individual peaks, it appears that the blue and green light curves of sources D and A (southern and that above the flare arcade) show some similarity to DPS and hard X-rays around 15:51:30 UT. However, in such a comparison it is necessary to take into account that the hard X-rays, EOVSA radio and DPS are generated by quite different emission mechanisms: by bremsstrahlung, gyrosychrotron, and plasma emission mechanisms, respectively. While the hard X-ray emission depends on the electron distribution of the superthermal electrons and the background plasma density, the EOVSA radio emission depends not only on the superthermal electron distribution, but on the magnetic field in the radio source. On the other hand,

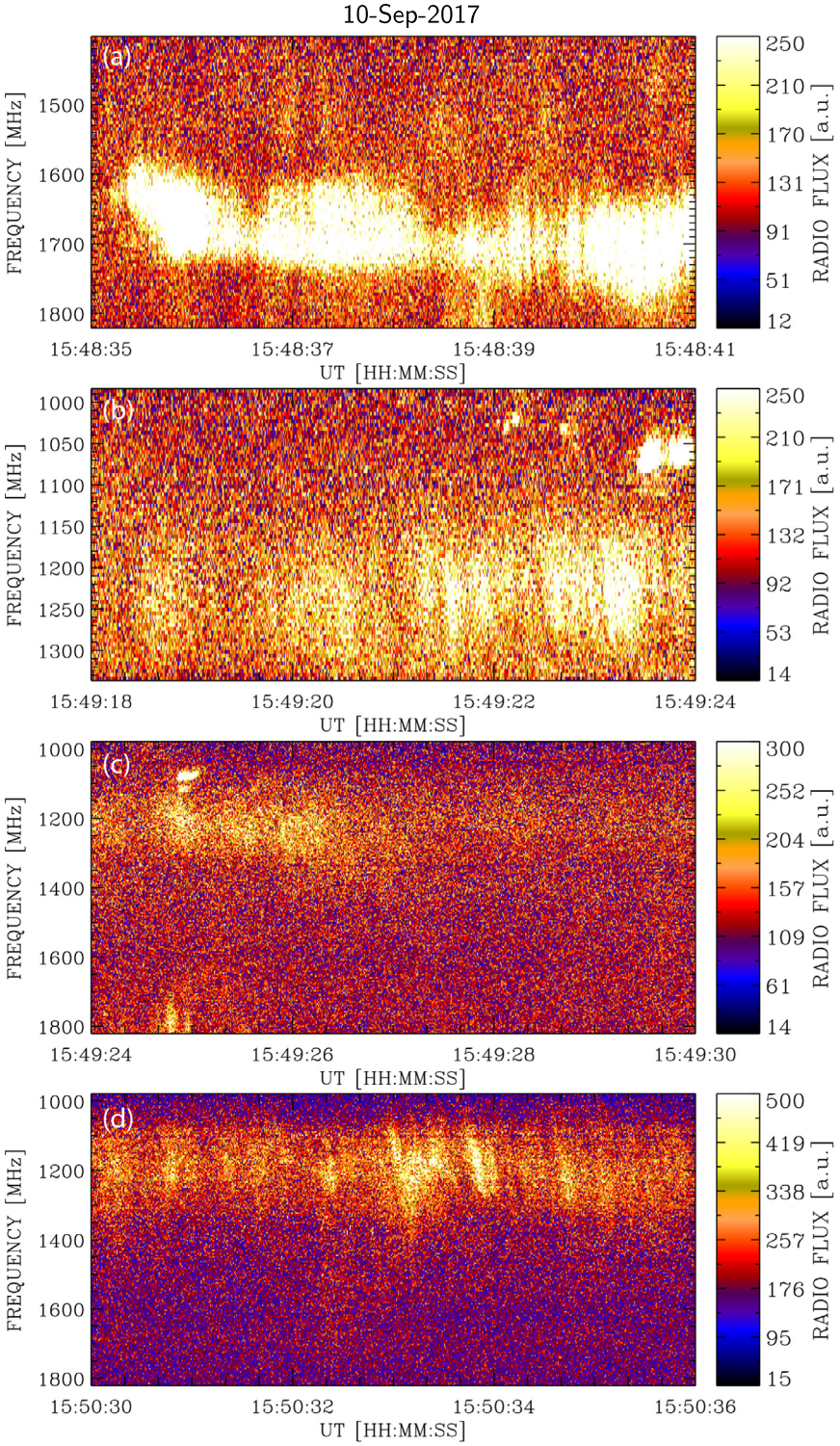

Figure 4. Four examples of the detailed 6 s radio dynamic spectra taken during the 15:48–15:54 UT time interval of the 2017 September 10 flare. See the white boxes labeled 4a, 4b, 4c, and 4d in Figure 1.

the brightness of the plasma emission depends on the derivative of the electron distribution in momentum space. At the start of DPS, there is no spatial HXR information available. (The first HXR image could be reconstructed no earlier than at 15:53 UT.) Figure 11 shows positions of the X-ray sources at this time. No further X-ray sources out of the field of view of this figure were found. Relative to the EOVSA radio sources, the X-ray sources are located only at comparatively low altitudes.

3. Interpretation

The most remarkable substructure is the double-band pulsations at the very beginning of DPS. Unfortunately, we do not have spatial observations at the DPS frequencies. Moreover, determination of the plasma density from EUV data in the assumed DPS source at this very early flare phase is not possible, due to the lack of appropriate data. Therefore, we

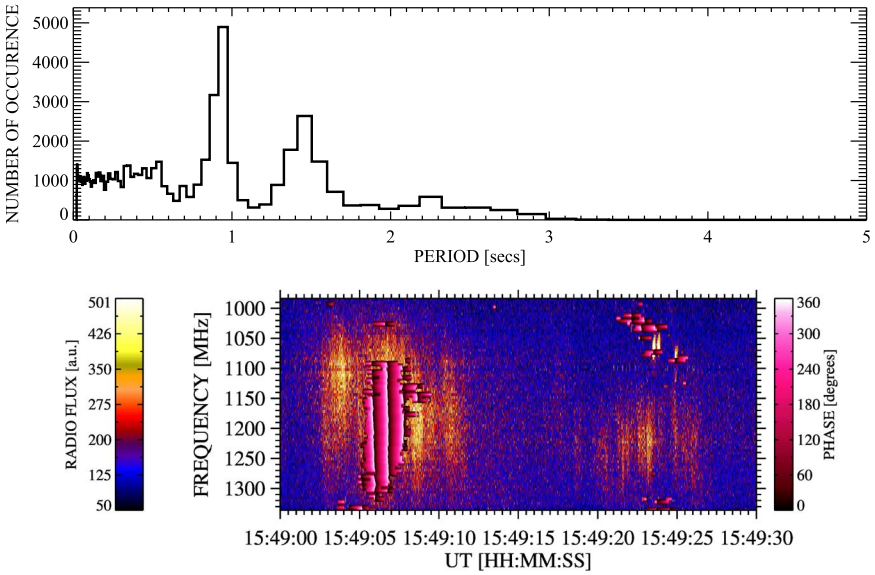

Figure 5. Histogram of periods in the spectrum observed at 15:49:00–15:49:30 UT (the spectrum in Figure 3(a)) and the corresponding phase maps (pink areas with the black lines showing the zero phase of oscillations) overplotted on the radio dynamic spectrum for periods detected in the range of 0.7–1.1 s.

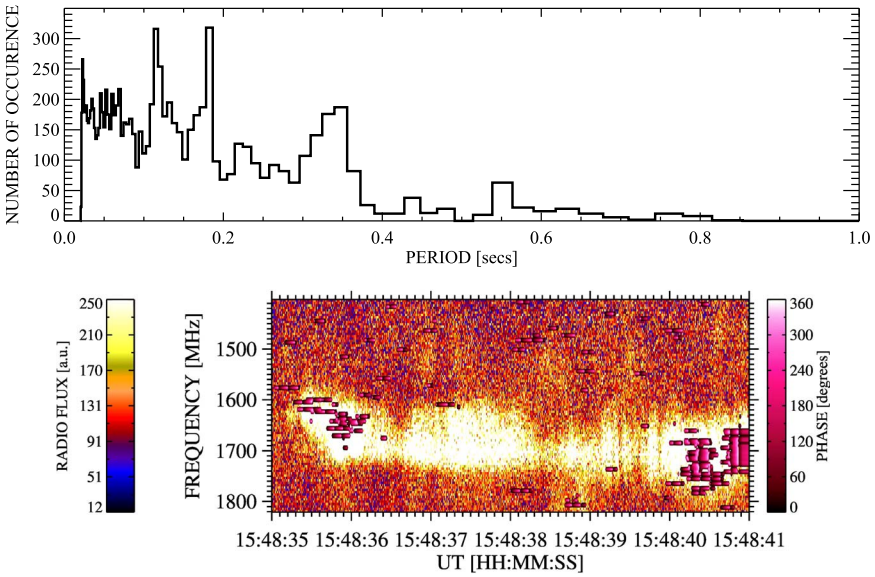

Figure 6. Histogram of periods in the spectrum observed at 15:48:35–15:48:41 UT (the spectrum in Figure 4(a)) and the corresponding phase maps (pink areas with the black lines showing the zero phase of oscillations) overplotted on the radio dynamic spectrum for periods detected in the range of 0.09–0.15 s.

interpret these double-band pulsations indirectly using the standard CSHKP flare model, previous observations of DPSs and results of numerical modeling of the magnetic reconnection. We also add further arguments in favor of our interpretation.

As already mentioned, comparing the positions of four (A, B, C, and D) EOVSA sources (Figure 9(a)) with the magnetic rope designated by the red dashed line in Figure 3 of Yan et al. (2018), we can see that source A is in the upper part of the magnetic rope, source B in the upper part of the flare arcade, and sources C and D near footpoints of the magnetic rope. According to the standard CSHKP flare model, the X-point of the flare magnetic reconnection, where particles are likely accelerated, is located between source A and B. From numerical modeling of the magnetic reconnection it is known that the accelerated electrons propagate from the X-point of the magnetic reconnection in the direction of the reconnection plasma outflows (Ricci et al. 2003; Pritchett 2006; Karlický 2008), i.e., in our case, upward in the solar atmosphere to source A, and downward to source B. The source in the upper part of the rising magnetic rope, i.e., source A, is referred to as a plasmoid. The plasmoid can be observed in X-rays as generated by the superthermal electrons by bremsstrahlung (Ohyama & Shibata 1998) and/or in radio, the present source A, or the 17 GHz plasmoid (Karlický & Kliem 2010) generated by the gyrosynchrotron mechanism. In papers by Kliem et al. (2000), Bárta et al. (2008a), it was shown that the superthermal electrons in such a plasmoid can also generate DPS.

Therefore, we assume that source A is also the source of the present DPS. Source A is the nonthermal source where there are the superthermal electrons which could generate DPS. Furthermore, comparing sources in Figure 8 at 15:48:24 and 15:49:08 UT with source A at 15:52:16 UT (Figure 9), we can

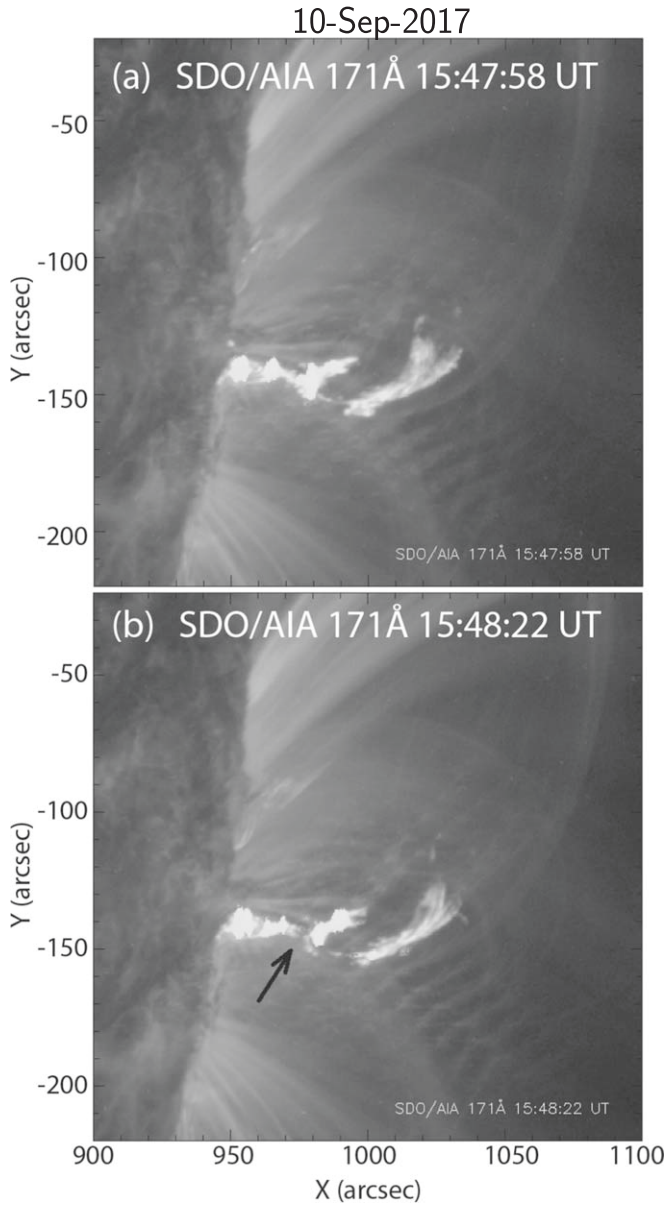

Figure 7. *SDO*/AIA 171 Å images at 15:47:58 and 15:48:22 UT during the 2017 September 10 flare, showing a tearing of the ejected filament, in the region marked by the black arrow, at 15:48:22 UT when on the radio spectrum the pulsations appeared in two frequency bands (Figure 2).

see that source A rises. It agrees with the negative drift of DPS; see also numerical simulations in Bárta et al. (2008b).

The magnetic reconnection below the rising filament starts when the current sheet is sufficiently narrow. Right at the beginning of magnetic reconnection, the distance between the magnetic rope and flare arcade is relatively small, therefore there is also small difference in plasma densities. At this moment, the electrons accelerated at the X-point of the magnetic reconnection move between the rising magnetic rope and the flare arcade and bombard the flare arcade as well as the magnetic rope. We think that this process exhibits in our observations as the double-band pulsations interconnected by the fast drifting bursts; see Figure 2. Namely, the superthermal electrons trapped in the magnetic rope and upper part of the flare arcade and along their trajectories between these traps generate the observed double-band pulsations and fast drifting bursts by the plasma emission mechanism.

This interpretation is supported by the observation of a tearing of the ejected filament at the same time as that of the double-band pulsations, and at the location where in the later time the flare current sheet was recognized, and a bifurcation of the lower-frequency source (<5.4 GHz) 40 s later (Figure 8(b)). Moreover, DPS in the 1000–1300 MHz as a whole drifts negatively, and the narrowband continuum in the 1600–1800 MHz range (Figure 4(a)), which belongs to the high-frequency part of the double-band pulsations, drifts positively. It expresses the upward motion of the rising magnetic rope to lower plasma densities and the increase of the plasma density in the arcade, respectively, which is in agreement with our interpretation.

As concerns sources C and D (Figure 9), our interpretation is that these sources are generated by the superthermal electrons propagating along the magnetic rope from the acceleration site (presumably located at or closed to source B according to the CSHKP scenario) by the gyrosynchrotron mechanism.

4. Discussion and Conclusions

In the paper, we present DPS with substructures (narrowband continua, drifting pulses, dot-like bursts) detected in DPSs for the first time. These different substructures indicate complex electron distribution functions in the DPS source. The drifting pulses could be associated with a beam-like distribution, whereas the pulsations and narrowband continua with a beam-like or/and loss-cone-type distribution. Thus, in the magnetic field of the magnetic rope these distributions can cause the plasmoid to be visible not only in the plasma emissions as substructures of DPS, but also in the gyrosynchrotron emission at frequencies above 3.41 GHz.

Using our new method based on the wavelet transform, we analyzed the periods in the time-frequency domain of DPS in detail. In most parts of DPS, we found periods around 1 s, which is in agreement with our previous studies. However, in the narrowband substructure at times between 15:48:35 and 15:48:41 UT, in the 1650–1750 MHz frequency band we detected new and very short periods in the 0.09–0.15 s range.

We presented positions of EOVSA sources observed in 3.4–12.4 GHz, their intensity evolutions and spectra at times of DPS. As followed from comparison of four EOVSA sources with the magnetic rope designated in Figure 3 in Yan et al. (2018), the EOVSA plasmoid (source A) coincides with the erupting magnetic rope. As shown in Figure 9(c), the spectra of the four microwave sources (as in Figure 9(a)) are likely nonthermal, with their peak brightness temperature in the 30–60 MK range. This indicates a presence of superthermal electrons in all of these sources. However, while the spectrum of source B is broadband, the spectra of the rest of the sources are relatively narrowband, and peak at lower frequencies. Assuming that the electron flux from the reconnection region upward to the flux rope and downward to the arcade is roughly the same then the question about the difference of spectra of the microwave sources arises. We assume that it is not only due to higher magnetic field strength in the arcade than that in the plasmoid, but also the arcade region likely has additional processes of energy release and particle acceleration.

Based on the standard CSHKP flare model and the previous observations of DPSs, we interpret that the EOVSA plasmoid (source A) is also the plasmoid where DPS is generated; see

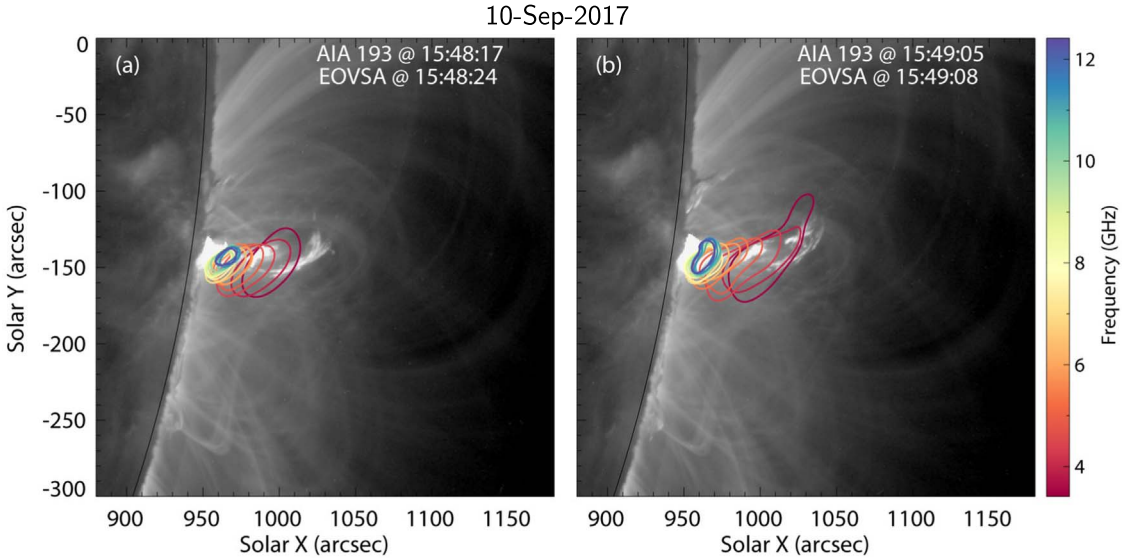

Figure 8. EOVSA sources (contours) at 15:48:24 and 15:49:08 UT during the 2017 September 10 flare, in the region of a tearing of the ejected filament.

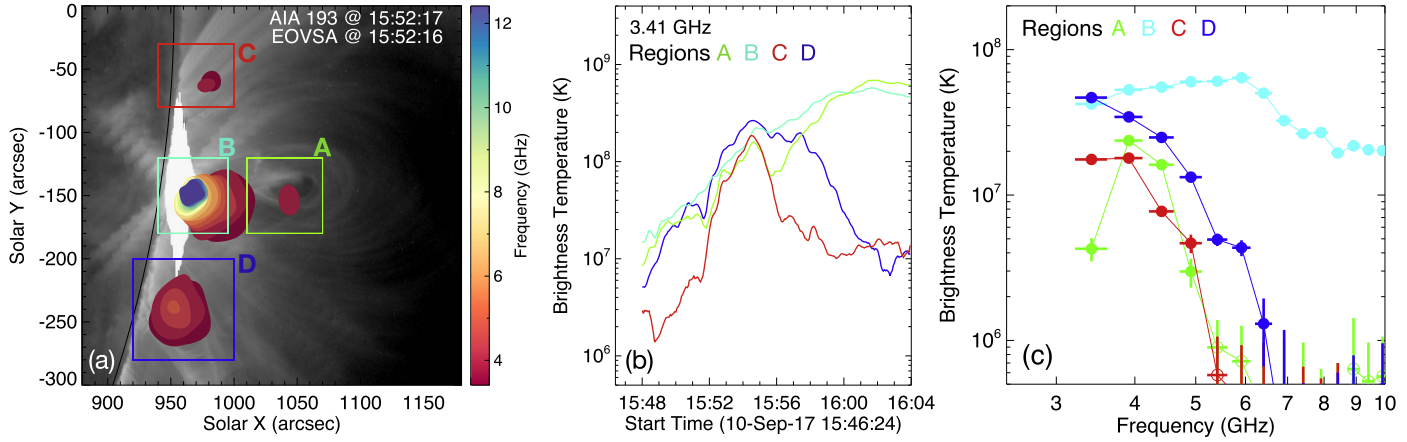

Figure 9. (a) EOVSA spectral imaging observation of the microwave sources in 3.4–12.4 GHz at 15:52:16 UT during the 2017 September 10 flare, with hues showing the sources at different frequencies (color bar). Background is *SDO*/AIA 193 Å image. (b) Time evolution of EOVSA 3.41 GHz maximum brightness temperature in four selected regions, marked with a box with the respective color in (a). (c) The corresponding spatially resolved brightness temperature spectra obtained near the center of each respective microwave sources.

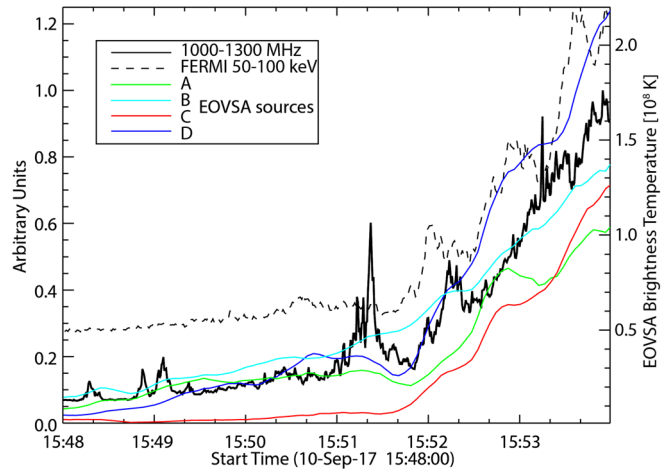

Figure 10. Radio flux in the 1000–1300 MHz range at 15:48–15:54 UT (black solid line) during the 2017 September 10 flare in comparison with the Fermi 50–100 keV X-ray flux (black dashed line) and the EOVSA light curves according to Figure 9(b).

Section 3. In this scenario, all periods found in DPS can be explained by the periodicity of electron acceleration in the magnetic reconnection below the magnetic rope as proposed by Kliem et al. (2000). However, there are other possibilities, e.g., that electron beam circulates in the magnetic field of the plasmoid, generating the plasma emission visible only from one side of the plasmoid, emitting the drifting pulses as in our case. In such a model, the period is given by the length of trajectory around the plasmoid divided by the beam velocity.

In our interpretation, the bulk of the nonthermal electrons are accelerated in or near the magnetic reconnection site located between the rising plasmoid (or the magnetic rope) and the flare arcade. Electrons trapped above the flare arcade produce the looptop HXR (blue contours in Figure 11) and microwave source (source B in Figure 9). Those precipitated at the footpoints give rise to the HXR footpoint source (blue and green contours near the solar limb in Figure 11). Some of the accelerated electrons are trapped in the flux rope/plasmoid (EOVSA source A in our case), and generate the emission at frequencies above 3.41 GHz by the gyrosynchrotron emission mechanism and also DPS by the plasma emission mechanism.

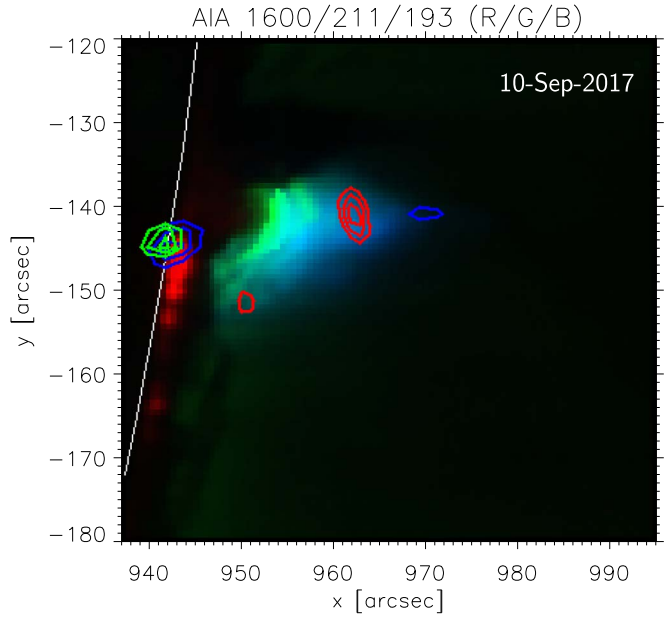

Figure 11. *RHESSI* sources at 15:53 UT during the 2017 September 10 flare superimposed on the 1600 Å (red), 211 Å (green), and 193 Å (blue) *SDO*/AIA images: 6–9 keV (red contours, 50%, 70%, 90%), 25–50 keV (blue contours), 50–100 keV (green contours). The presented field of view corresponds roughly to the cyan box B in Figure 9(a).

The accelerated electrons in the flux rope may further escape and propagate to the footpoints of the flux rope, which we adopt as one possible interpretation for the presence of the two EOVSA microwave side sources (sources C and D in Figure 9), as well as the apparent similarity in their light curves with the central EOVSA microwave sources (sources B and A), the DPS, and X-ray emission during the initiation phase of the flare (prior to ∼15:54 UT; Figure 10). The observation of these side sources is somewhat similar to the microwave source observed by NoRH at 17 GHz that appeared to coincide with a hot magnetic rope (seen by AIA 131 Å) during the preimpulsive stage of an eruptive 2012 July 19 flare (Wu et al. 2016), although the peak brightness temperature of their 17 GHz microwave source was less than only 20 kK and spectral information was not available.

This scenario agrees with our unique observation of the pulsations in two separate bands in the 1000–1300 and 1600–1800 MHz ranges, just at the moment of tearing of the ejected filament in the region, where in later times a signature of the flare current sheet appears (Figures 2, 7, and 8). We interpret the pulsations at these two bands as the plasma emission from the flux rope (1000–1300 MHz) and that from the top of the flare arcade (1600–1800 MHz). Assuming that the radio emission of these two bands of DPS at about 15:48:20 UT are emitted on the fundamental frequency, the plasma density in the flux rope at this early flare phase is in the range of 1.23×10^{10}–$2.08 \times 10^{10}\,\mathrm{cm}^{-3}$ and in the arcade top is 3.16×10^{10}–$4.00 \times 10^{10}\,\mathrm{cm}^{-3}$. Note that these plasma densities are in the interval between the densities estimated in the flare arcade at 15:59 UT, i.e., at about 10 minutes after DPS, $((0.9–2.0) \times 10^{11}\,\mathrm{cm}^{-3}$ Polito et al. 2018) and the plasma density in the current sheet ($10^{10}\,\mathrm{cm}^{-3}$ Warren et al. 2018). Because the density in the arcade increases during the flare and the density in the DPS source is expected to be similar to that in the current sheet, the estimated densities support our interpretation. It is interesting that the pulsations in these two bands are interconnected by fast drifting bursts. We propose that they are generated by superthermal electrons propagating between the pulsation regions. Moreover, DPS in the 1000–1300 MHz as a whole drifts negatively and the narrowband continuum in the 1600–1800 MHz range, with the shortest period found (0.09–015 s) drifts positively. It expresses the upward motion of the rising magnetic rope to lower plasma densities and the increase of the plasma density in the arcade, respectively, in agreement with our interpretation.

We acknowledge support from the project RVO-67985815 and GA ČR grants 17-16447S, 18-09072S, and 19-09489S. D. G. and B.C. acknowledge support from NSF grant AST-1910354, AGS-1654382, and NASA grants 80NSSC18K1128, 80NSSC19K0068, and NNX17AB82G to NJIT. This work was also supported by the Science Grant Agency project VEGA 2/0048/20 (Slovakia). Help from the Bilateral Mobility Projects SAV-18-01 of the SAS and CAS is acknowledged. This article was created in the project ITMS No. 26220120029, based on the supporting operational Research and development program financed from the European Regional Development Fund. We acknowledge the use of the *Fermi* Solar Flare Observations facility funded by the *Fermi* GI program (http://hesperia.gsfc.nasa.gov/fermi_solar/).

ORCID iDs

Marian Karlický https://orcid.org/0000-0002-3963-8701
Bin Chen https://orcid.org/0000-0002-0660-3350
Dale E. Gary https://orcid.org/0000-0003-2520-8396
Jana Kašparová https://orcid.org/0000-0001-9559-4136
Jan Rybák https://orcid.org/0000-0003-3128-8396

References

Aurass, H., Mann, G., Zlobec, P., & Karlický, M. 2011, ApJ, 730, 57
Bárta, M., Karlický, M., & Žemlička, R. 2008a, SoPh, 253, 173
Bárta, M., Vršnak, B., & Karlický, M. 2008b, A&A, 477, 649
Carmichael, H. 1964, NASSP, 50, 451
Gary, D. E., Chen, B., Dennis, B. R., et al. 2018, ApJ, 863, 83
Gopalswamy, N., Yashiro, S., Mäkelä, P., et al. 2018, ApJL, 863, L39
Hirayama, T. 1974, SoPh, 34, 323
Isliker, H., & Benz, A. O. 1994, A&AS, 104, 145
Jiřička, K., & Karlický, M. 2008, SoPh, 253, 95
Jiřička, K., Karlický, M., Kepka, O., & Tlamicha, A. 1993, SoPh, 147, 203
Karlický, M. 2008, ApJ, 674, 1211
Karlický, M., & Bárta, M. 2007, A&A, 464, 735
Karlický, M., Fárník, F., & Krucker, S. 2004, A&A, 419, 365
Karlický, M., & Kliem, B. 2010, SoPh, 266, 71
Karlický, M., & Rybák, J. 2017, SoPh, 292, 1
Karlický, M., Rybák, J., & Bárta, M. 2018, SoPh, 293, 62
Karlický, M., Rybák, J., & Monstein, C. 2017, SoPh, 292, 94
Khan, J. I., Vilmer, N., Saint-Hilaire, P., & Benz, A. O. 2002, A&A, 388, 363
Kliem, B., Karlický, M., & Benz, A. O. 2000, A&A, 360, 715
Kliem, B., Linton, M. G., Török, T., & Karlický, M. 2010, SoPh, 266, 91
Kliem, B., & Török, T. 2006, PhRvL, 96, 255002
Kopp, R. A., & Pneuman, G. W. 1976, SoPh, 50, 85
Lemen, J. R., Title, A. M., Akin, D. J., et al. 2012, SoPh, 275, 17
Lin, R. P., Dennis, B. R., Hurford, G. J., et al. 2002, SoPh, 210, 3
Long, D. M., Harra, L. K., Matthews, S. A., et al. 2018, ApJ, 855, 74
Loureiro, N. F., Schekochihin, A. A., & Cowley, S. C. 2007, PhPl, 14, 100703
Meegan, C., Lichti, G., Bhat, P. N., et al. 2009, ApJ, 702, 791
Nishizuka, N., Karlický, M., Janvier, M., & Bárta, M. 2015, ApJ, 799, 126
Ohyama, M., & Shibata, K. 1998, ApJ, 499, 934
Omodei, N., Pesce-Rollins, M., Longo, F., Allafort, A., & Krucker, S. 2018, ApJL, 865, L7
Polito, V., Dudík, J., Kašparová, J., et al. 2018, ApJ, 864, 63
Pritchett, P. L. 2006, JGRA, 111, A10212
Ricci, P., Lapenta, G., & Brackbill, J. U. 2003, PhPl, 10, 3554

Sturrock, P. A. 1966, Natur, 211, 695
Tan, B., Tan, C., Zhang, Y., et al. 2014, ApJ, 790, 151
Veronig, A. M., Podladchikova, T., Dissauer, K., et al. 2018, ApJ, 868, 107
Warren, H. P., Brooks, D. H., Ugarte-Urra, I., et al. 2018, ApJ, 854, 122
Wu, Z., Chen, Y., Huang, G., et al. 2016, ApJL, 820, L29
Yan, X. L., Yang, L. H., Xue, Z. K., et al. 2018, ApJL, 853, L18